

# Turbulent Noise Sources Reduction by LEBU and Riblets

Chioma Muhammad\* and Tze Pei Chong<sup>†</sup>  
Brunel University London, Uxbridge, UB8 3PH, UK

An experimental study is presented on the application of Large Eddy BreakUp (LEBU) on a flat plate as an outer layer source-targeting device to mitigate the wall pressure fluctuations and lateral coherence length scale of a turbulent boundary layer developed at zero pressure gradient. Both represent the prominent noise sources for the trailing edge noise radiation. When a LEBU is placed strategically at the outer part of a turbulent boundary layer, the wall pressure spectra can establish a self-similar behaviour against  $s'$ , which is a normalised separation distance between the LEBU's trailing edge and the targeted location for noise mitigation. It is found that  $s'$  has to be greater than 3 to achieve an overall reduction in the wall pressure fluctuations. What appears to be the optimal LEBU configuration for the mitigation of wall pressure fluctuations, however, will not be reciprocated in the lateral coherence length. The combined effect would render the LEBU rather ineffective to reduce the frequency-integrated, overall noise radiation. Our previous study has confirmed that riblets, a near wall source-targeting device, is more effective in the mitigation of the lateral coherence length. Under the principle of non-interference, a combination of Riblets and LEBU (RIBU) demonstrates that reduction of the frequency-integrated, overall noise radiation can be achieved, again at  $s' > 3$ .

## Nomenclature

$f$	=	frequency, Hz
$h$	=	height of the riblets protuberance, mm
$\tilde{h}$	=	vertical distance between LEBU's trailing edge and wall surface, mm
$H$	=	shape factor
$s'$	=	$(\overleftarrow{\Delta x}/\delta_o + \overrightarrow{\Delta x}/\delta_o)$ , normalised distance between LEBU's trailing edge and targeted location for mitigation
$S$	=	lateral separation distance of the protuberances for the riblets, mm
$s_{pp}$	=	far field acoustic pressure, Pa
$s_{qq}$	=	wall pressure power spectral density, Pa

\*Research Engineer, Dyson, Chioma.Muhammad@gmail.com, Non-AIAA Member.

<sup>†</sup>Professor, Department of Mechanical and Aerospace Engineering, t.p.chong@brunel.ac.uk, AIAA Senior Member.

Presented as Paper 2023-3336 at the AIAA Aviation 2023 Forum, San Diego, California, 12-16 June 2023.

$S_{qq}$	= overall, frequency-integrated wall pressure fluctuation, Pa
$t'$	= time of flight of turbulent spots (normalised)
$u_\tau$	= friction velocity, $\text{ms}^{-1}$
$\tilde{u}$	= velocity perturbation (normalised)
$u'$	= root-mean-square velocity fluctuation (normalised)
$U_\infty$	= freestream velocity, $\text{ms}^{-1}$
$x, y, z$	= streamwise, wall-normal and lateral directions, mm
$X_{\text{ref}}$	= reference location at $x = 625$ mm
$\overleftarrow{\Delta x}$	= upstream LEBU distance from $X_{\text{ref}}$ , mm
$\delta$	= boundary layer thickness, mm
$\delta^*$	= boundary layer displacement thickness, mm
$\gamma_z^2$	= lateral coherence function between two microphone signals
$\nu$	= kinematic viscosity, $\text{m}^2 \text{s}^{-1}$
$\Phi$	= cross power spectral density between two microphone signals
$\theta$	= boundary layer momentum thickness, mm
$\overrightarrow{\Delta x}$	= downstream microphone distance from $X_{\text{ref}}$ , mm
Subscripts	
$b$	= baseline case
$l$	= LEBU case
$\circ$	= reference location ( $x = X_{\text{ref}}$ )
$r$	= RIBU case
spot	= turbulent spot case

## I. Introduction

ONE of the major noise sources for an aerofoil is the trailing edge self-noise [1], which has received much attention from the wind turbine and aviation industries. When the boundary layer has undergone a complete transition to fully turbulent at the trailing edge, a cascade of turbulent length scale eddies are scattered into a broad frequency band of acoustic disturbances into the far field. By solving the Lighthill equation based on a half-plane Green's function, Ffowcs Williams and Hall [2] obtained an expression of the scattered acoustic pressure by the vortical velocity field around the trailing edge. They also derived a general scaling law for the acoustic power radiated from a solid edge as having a velocity dependence to the fifth power. In other words, the same isolated turbulent eddies will scatter into noise more efficiently at the edge than in domains far from the edge. Amiet [3] and Howe [4] took a slightly different

approach of the trailing edge noise formulation by linking the far field acoustic power spectral density to both the wall pressure spectra and lateral coherence length spectra near the trailing edge. Essentially, these hydrodynamics sources are treated as an equivalent acoustic sources that are originated from the vortical velocity field. For the most recent review paper on the theoretical, numerical and experimental developments of the understanding of trailing edge noise, readers can refer to Lee *et al.* [5].

An effective strategy for the mitigation of the radiated turbulent broadband trailing edge noise is to execute the *source targeting* through manipulation, alteration or prevention of the growth mechanisms of turbulent boundary layer. More specifically, efforts to execute the source targeting can focus on either the inner part, or the outer part of a turbulent boundary layer, respectively. Recently, we disseminated some results on the use of riblets to target the inner part of turbulent boundary layer for the mitigation of turbulent noise sources on a flat plate system [6]. Although no acoustic results are available, the near-wall turbulence structures are found to dissipate quite rapidly when crossing the riblets surface. The riblets can slightly reduce the fluctuating wall pressure power spectral density level at the low and high frequency ranges, but they will also cause an increase at the mid frequency range. On the other hand, the lateral turbulence coherence length scale across a large frequency range can be reduced by the riblets. The combined effects give rise to an effective mitigation of the turbulent noise source at the low and high frequency regions by the riblets, potentially transferable to the trailing edge noise reduction.

A classical outer layer manipulator is the Large Eddy Break Up (LEBU) devices, which consist of a two-dimensional thin plate or aerofoil placed onto the outer part of a turbulent boundary layer. They are placed in such a way that the wake emanated from the LEBU can disrupt the turbulence structure self-sustaining mechanisms of momentum transport into the boundary layer downstream. The aim is to target large turbulent eddies in the boundary layer, and break them up into smaller, lower energy eddies that will eventually be dissipated by the viscosity [7]. Hefner *et al.* [8] utilise a number of horizontal plates suspended over the flow surface so that there is interaction with the outer layer of the boundary layer. They observe a 24% reduction of skin friction over a longitudinal range of 45 device heights, although a net drag reduction cannot be realised presumably due to the increased parasite drag incurred by the supporting struts of the LEBU. Based on their velocity fluctuating spectra, Savill and Mumford [9] describe the penetration of small scale turbulent eddies to the boundary layer via the wake of the LEBU, which also acts as a shield to prevent incursions of high speed fluid from the outer layer to the near wall region. A large eddy simulation is performed by Chin *et al.* [10], who observe skin friction reduction over a considerable distance downstream of the LEBU. They attribute this to the breakup of high and low momentum bulges by the LEBU, followed by a shift in large-scale energy into smaller-scale eddies. The mechanism by which the LEBU can reduce the turbulence has recently been investigated by Chong and Muhammad [11]. They found that while the oscillatory wake emanated from the LEBU can help to inhibit the turbulent fluid ejection at the near wall, effective disruption of the wall sweeping event can only be achieved when the LEBU is placed at least  $3\delta_o$  upstream of the target location, where  $\delta_o$  is the local turbulent boundary layer thickness.

The previous works on the LEBU as an outer layer device for turbulent drag reduction suggest that it has a potential to execute an effective source targeting to achieve turbulent self-noise reduction. This paper will investigate the potential of LEBU for the reduction of turbulent wall pressure sources that are important for aerofoil self-noise radiation. To the best knowledge of the authors, the change in the turbulence structures by LEBU has not been studied much from the perspectives of the wall pressure fluctuation field. Furthermore, it still remains relatively scarce in the literature that describes the turbulence spectral characteristics produced by LEBU, including the manipulation of the turbulence lateral coherence length scale. This paper aims to shed some lights on LEBU for their potential to be a trailing edge self-noise reduction device. Determining the normalised streamwise separation distance between the LEBU's trailing edge and the targeted location for noise mitigation represents another objective of this work.

Another avenue to enhance the source targeting is to tackle both the inner and outer parts of a turbulent boundary layer, simultaneously. Walsh and Lindemann [12] placed riblets downstream of the LEBU to investigate the combined effect of the drag reduction devices. They observe that the net level of drag reduction achieved by both devices is additive in general. This suggests that the riblets and LEBU will not interfere negatively against each other. A similar phenomenon is also reported by Gudilin *et al.* [13] where a total of 16% skin friction reduction can be achieved. This paper will explore a combination of Riblets and LEBU, i.e. which can be abbreviated as the RIBU, for their effectiveness to enhance the source targeting to mitigate turbulent noise sources.

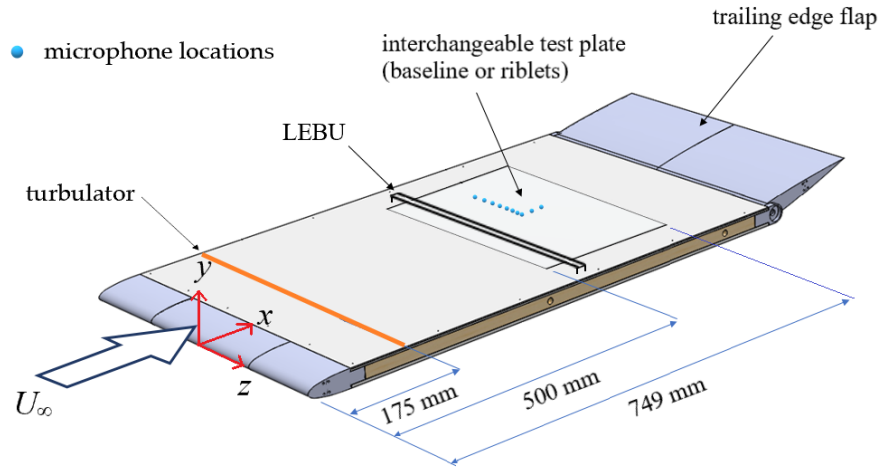


**Fig. 1** Schematic showing the flat plate model used in the current study. The coordinate system is also shown. Drawing is not to scale.

## II. Experimental Setup

The experiments were conducted in an open circuit, suction type wind tunnel where the axial fan is driven by a 7.5 kW motor capable of achieving velocity up to  $35 \text{ ms}^{-1}$  inside the  $0.5 \times 0.5 \text{ m}$  working section. The walls are constructed by Perspex to allow optical access. The mean turbulence intensity of the freestream flow is measured to be

less than 0.5%.

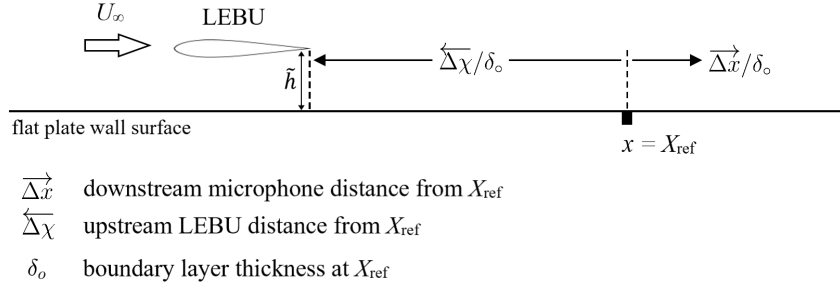


**Fig. 2 Schematic showing the LEBU arrangement. Drawing is not to scale.**

### A. Design of a flat plate system with LEBU

The flat plate system developed by Muhammad and Chong [6], which features a semi-hollow section for interchangeable test plates (baseline smooth surface and riblets), is also utilised in this study. As illustrated in Figure 1, the flat plate system is described by a coordinate system of  $x$ ,  $y$  and  $z$ , which represents the streamwise, wall-normal, and lateral directions, respectively. In the figure,  $x = 0$  marks the leading edge of the flat plate. A trailing edge flap is incorporated to control the front stagnation point, ensuring smooth boundary layer development on the upper flow surface. A zig-zag turbulator is positioned at  $x = 175$  mm to serve as a passive device for artificially generating a two-dimensional turbulent boundary layer. The turbulator has a width of 8.1 mm covering the whole span of the flat plate, and a maximum thickness of 1.2 mm.

$\overleftarrow{\Delta \chi}$ (mm)	5	15	30	50	80
$\overleftarrow{\Delta \chi} / \delta_o$ at $10 \text{ m s}^{-1}$	0.440	1.321	2.643	4.405	7.047
$\overleftarrow{\Delta \chi} / \delta_o$ at $12 \text{ m s}^{-1}$	0.461	1.382	2.763	4.605	7.369
$\overleftarrow{\Delta \chi} / \delta_o$ at $15 \text{ m s}^{-1}$	0.476	1.428	2.856	4.761	7.617

**Table 1 Dimensional ( $\overleftarrow{\Delta \chi}$ ) and non-dimensional ( $\overleftarrow{\Delta \chi} / \delta_o$ ) distances of the LEBU's trailing edge placement in the upstream direction from  $X_{\text{ref}}$ .**

An illustration of the LEBU system is shown in Figure 2. The LEBU is a NACA0014 symmetrical aerofoil with chord length  $C_{\text{LEBU}} = 15$  mm, which entails a maximum thickness of approximately 2 mm to resemble a thin, but also sturdy device. The LEBU is supported by struts that are laser-cut from 0.5 mm thick plywood. Two different heights of struts have been used in this study, which will raise the centreline and trailing edge of the LEBU to a height of  $\tilde{h} = 2.5$  mm and 5.0 mm above the surface of the flat plate, henceforth referred to the LEBU<sub>2.5</sub> and LEBU<sub>5.0</sub>, respectively. The struts carrying the entire LEBU are movable in the streamwise direction, which will be described by a non-dimensional

distance of  $\overleftarrow{\Delta x}/\delta_o$  as depicted in Figure 2. With the designation that the main flow is from left to right, the overhead left arrow in  $\overleftarrow{\Delta x}$  emphasises the direction of which the LEBU is moved upstream from a reference location,  $X_{\text{ref}}$ , where  $X_{\text{ref}} = x = 625$  mm.  $\delta_o$  is the boundary layer thickness measured at  $X_{\text{ref}}$ . As a summary,  $\overleftarrow{\Delta x}/\delta_o$  is a non-dimensional distance between  $X_{\text{ref}}$  and the LEBU's trailing edge. In this study, there are total of five  $\overleftarrow{\Delta x}$  locations tested under three freestream velocities  $U_\infty = 10, 12$  and  $15 \text{ m s}^{-1}$ . The tabulated values can be found in Table 1.

$\overrightarrow{\Delta x}$ (mm)	0 ( $X_{\text{ref}}$ )	20	40
$\overrightarrow{\Delta x}/\delta_o$ at $10 \text{ m s}^{-1}$	0	1.762	3.524
$\overrightarrow{\Delta x}/\delta_o$ at $12 \text{ m s}^{-1}$	0	1.842	3.684
$\overrightarrow{\Delta x}/\delta_o$ at $15 \text{ m s}^{-1}$	0	1.904	3.808

**Table 2 Dimensional ( $\overrightarrow{\Delta x}$ ) and non-dimensional ( $\overrightarrow{\Delta x}/\delta_o$ ) distances of the measurement locations in the downstream direction from  $X_{\text{ref}}$ .**

For the test plate system, a recess between  $500 \leq x \leq 749$  mm is designed to accommodate either a baseline smooth surface test plate or a riblets surface test plate, both of which have the same overall length. The baseline test plate features a smooth aluminum finish achieved through 3-axis CNC machining. This plate includes arrays of 0.4 mm diameter pressure tap holes distributed in the streamwise and lateral directions for measuring wall pressure fluctuations. The streamwise locations of these pressure taps are  $x = 625$  ( $X_{\text{ref}}$ ), 627, 634, 645, 655, 665, 685 and 725 mm, all of whom will be used simultaneously to measure the convection rates of the turbulent eddies. For the discussion of the wall pressure spectra results in the remaining sections, however, only three streamwise locations ( $x = 625$  ( $X_{\text{ref}}$ ), 645, and 665 mm) will be considered. They are expressed as  $\overrightarrow{\Delta x} = 0, 20$  and  $40$  mm, respectively, where the overhead right arrow emphasises the direction of which the measurement location is located downstream from  $X_{\text{ref}}$ , as depicted in Figure 2. In what follows, they will be non-dimensionalised by the boundary layer thickness measured at the reference location, giving rise to a notation of  $\overrightarrow{\Delta x}/\delta_o$  as summarised in Table 2.

Combining the LEBU placements in Table 1 with the targeted locations for noise mitigation in Table 2 will give rise to 45 unique combinations of  $s' = (\overleftarrow{\Delta x}/\delta_o + \overrightarrow{\Delta x}/\delta_o)$ .  $s'$  is therefore a non-dimensional separation distance between the LEBU's trailing edge and the targeted location for noise source mitigation. Choosing the baseline boundary layer thickness at  $X_{\text{ref}}$  as the scaling factor is an effective strategy for the generalisation of the LEBU performance. This is particularly valid for zero or favourable pressure gradient flow when the rates of growth of the boundary layer thickness are relatively low.

The flat plate also contains multiple pressure taps in the lateral direction to measure the lateral coherence length of the turbulence. This particular lateral array is situated at  $x = X_{\text{ref}}$ , where the lateral spacing is  $\Delta z = 2.0, 4.2, 6.6, 9.2, 12.0, 15.0$  and  $18.2$  mm from the central of the test plate.

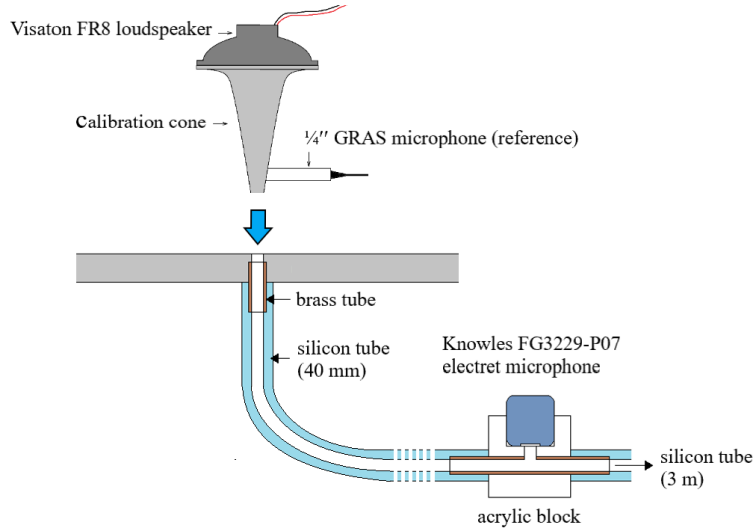


**Fig. 3** The remote microphone configuration and calibration system. Reprinted from “Mitigation of turbulent noise sources by riblets” by Muhammad and Chong, 2022, *Journal of Sound and Vibration* 541, 117302, with permission from Elsevier.

## B. Instrumentation

Knowles FG3229-P07 electret microphones, which are circular with a diameter of 2.57 mm and a sensing diameter of 0.8 mm, have been used for measuring wall pressure fluctuations. As shown in Figure 3, the microphone is mounted remotely beneath the wall surface using an acrylic holder and is connected to the wall surface via a 40 mm silicone tube. Another silicone tube, approximately 3 m long, is connected to the other end of the acrylic holder and extends out of the wind tunnel’s working section. This long tube ensures that the acoustic waves traveling inside the remote microphone system do not encounter a sudden termination, which would cause backward reflections and potentially create standing waves, resulting in spurious fluctuations in the power spectral density. This remote microphone configuration also ensures that the 0.4 mm pinhole diameter of the wall surface is maintained throughout the tubing system. Care is taken to minimise curvature and bends in each tube connecting the wall surface to the acrylic holder to reduce pressure loss.

A Visaton FR8 10W full-range speaker is used to calibrate each remote microphone *in-situ*. It is attached to a cone designed to direct sound pressure waves from a larger area to a smaller one. A similar calibration method was used in other studies [14, 15]. In this method, a 1/4" GRAS reference microphone with a known frequency response is embedded in the cone wall near the surface, as shown in Figure 3. This setup allows simultaneous measurement of signals from the remote microphone and the reference microphone, enabling the determination of the phase function for each remote microphone. During the experiment, raw data from each remote microphone is sampled at 40 kHz for 15 seconds, totaling 600,000 samples. The data acquisition system has a 16-bit resolution, and each sampling channel includes a built-in anti-aliasing filter.

These remote microphone sensors are phase-calibrated against the calibration cone to allow accurate analysis of

the cross-correlation and coherence functions from the acquired signals. Note that the amplitude of the fluctuations is not calibrated for the remote microphone sensors. However, once installed, these remote microphone sensors remain undisturbed, making direct comparisons of wall pressure power spectral density between the baseline and LEBU cases valid.

Flow velocity fluctuations are measured using a miniature single hot wire (Dantec 55P11), which has a 1.25 mm long, 5  $\mu\text{m}$  diameter tungsten sensing wire. Operated by a constant temperature anemometer, the hot wire's overheat ratio is set to 1.8, resulting in an operating temperature of approximately 300°C. The hot wire is attached to a three-axis traverse system with step motors capable of achieving very fine movements of 0.01 mm, providing the high spatial resolution needed for boundary layer measurement. The analogue-to-digital (A/D) card used in the hot wire acquisition has a 12-bit resolution. Data is sampled at 20 kHz for 13 seconds, and a low-pass filter of 10 kHz is used to ensure the sampled signal remains within the Nyquist frequency and is not contaminated by aliasing. Temperature correction of the sampled hot wire signals is performed during post-analysis.

$U_\infty$ (m s <sup>-1</sup> )	$\delta_o$ (mm)	$\delta_o^*$ (mm)	$\theta_o$ (mm)	$H$
10	11.352	1.849	1.362	1.358
12	10.857	1.776	1.314	1.351
15	10.503	1.688	1.260	1.340

**Table 3** Summary of the turbulent boundary layer parameters at  $X_{\text{ref}}$  for the baseline flat plate.

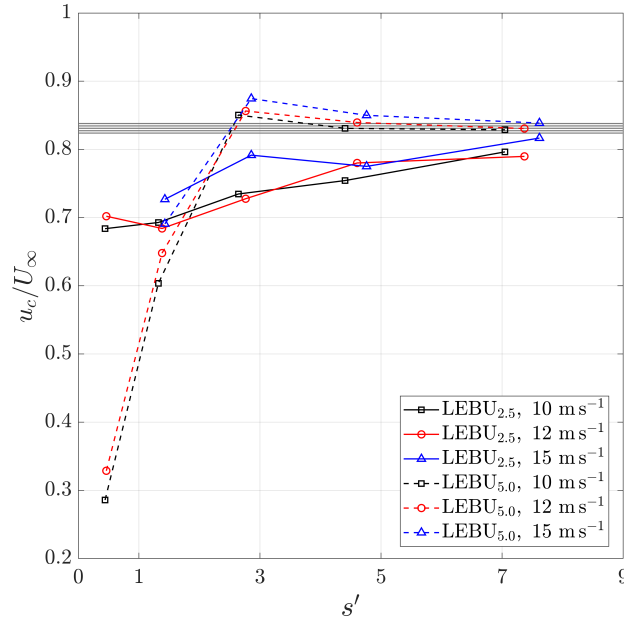


**Fig. 4** Convection velocities of the large-scale turbulence eddies. The datum range produced by the baseline flat plate is indicated by the multiple horizontal lines.

### III. Wall Pressure Turbulence subjected to LEBU

The results presented here can provide a basis for the LEBU to reduce aerofoil trailing edge self-noise ultimately. The measurement campaign includes experiments conducted at three freestream velocities,  $U_\infty = 10, 12$  and  $15 \text{ ms}^{-1}$  to facilitate a sensitivity study for the spatial distributions of LEBU ( $\tilde{h}$  and  $\overleftarrow{\Delta\chi}/\delta_o$ ) and their effects on the wall pressure turbulent noise sources production. Table 3 summarises the turbulent boundary layer parameters at  $x = X_{\text{ref}}$  for the baseline flat plate. In the table,  $\delta_o, \delta_o^*$  and  $\theta_o$  denote the baseline's boundary layer thickness, displacement thickness and momentum thickness, respectively, at  $X_{\text{ref}}$ . The shape factors,  $H$ , typically fall between 1.3 and 1.4, confirming the establishment of fully-developed turbulent boundary layer across all the measurement points in the current study.

At  $U_\infty = 10, 12$  and  $15 \text{ ms}^{-1}$ , the LEBU<sub>2.5</sub> entails  $\tilde{h}u_\tau/\nu \approx 85, 100$  and  $120$ , and  $\tilde{h}/\delta_o \approx 0.22, 0.23$  and  $0.24$ , respectively, at  $X_{\text{ref}}$ . This can be considered as a source targeting on the inner region of turbulent boundary layer. Note that  $\nu$  is the kinematic viscosity, and  $u_\tau$  is the local friction velocity determined from the measured baseline velocity profiles at  $X_{\text{ref}}$  by the Clauser method. On the other hand, LEBU<sub>5.0</sub> will locate at wall-normal distances twice the values of the  $\tilde{h}u_\tau/\nu$  and  $\tilde{h}/\delta_o$  described above, resulting in a source targeting device that focuses on the outer region of the turbulent boundary layer at  $X_{\text{ref}}$ .

#### A. Turbulence wall pressure convection

A cross-correlation in the spatial-temporal domain for the longitudinal wall pressure fluctuations is conducted. The output of this analysis is the cross-correlation coefficient  $R_{x_i x_j}$  as a function of time delay between signals,  $\tau$ , which can be used to determine the convection velocity of the most prevalent scale of turbulence structures. In the present experiments, all the streamwise cross-correlation studies were conducted by taking reference to the most upstream microphone sensor at  $x = X_{\text{ref}} = 625 \text{ mm}$ . The convection time for the most dominant wall pressure generating structures to traverse between them can be identified by the  $\tau_{\text{max}}$  corresponding to the maximum cross-correlation coefficient  $R_{x_i x_j \text{max}}$ . From a dataset of  $(\overrightarrow{\Delta x}, \tau_{\text{max}})$ , an average convection velocity of the dominant turbulent eddies can be determined. It should be noted that the most dominant turbulent eddies in the boundary layer would decay at a slower rate than the small-scale turbulent eddies.

Figure 4 shows the normalised convection velocities of the turbulence eddies  $u_c/U_\infty$ , as a function of  $s'$ , at  $U_\infty = 10, 12$  and  $15 \text{ ms}^{-1}$ . The figure demonstrates that the LEBU can slow down the longitudinal turbulence convection considerably for both the LEBU<sub>2.5</sub> and LEBU<sub>5.0</sub> types, but will eventually recover to the baseline datum as the  $s'$  increases. The deviation from the baseline datum is the most significant at low  $s'$ , i.e. when the LEBU is at the closest proximity to  $X_{\text{ref}}$ . This illustrates that the velocity deficit of the near wake emanated from the LEBU can exert a retarding impact to cause a slow down of the local turbulence convection.

The reduction in turbulence convection is the most pronounced for the LEBU<sub>5.0</sub> case, where a reduction down to  $u_c/U_\infty \approx 0.3$  is observed. However, what appears to be a significant reduction in turbulence convection at low  $s'$

initially will be followed by a steep recovery to return to the baseline level as  $s'$  increases, i.e. the LEBU moves further upstream and away from  $X_{\text{ref}}$ . It is also worth noting that in almost all cases an overshoot in the turbulence convection appears at  $2.5 \leq s' \leq 4.5$ , before returning to the baseline level at  $s' > 5$ .

When the LEBU is lowered to  $\tilde{h} = 2.5$  mm (LEBU<sub>2.5</sub>), its emanated wake will predominantly interact with the inner region that is already characterised by low speed fluids. Hence it is not expected to fundamentally change the local velocity gradient and turbulence convection. While it still exhibits a reduction when the LEBU is situated near the  $X_{\text{ref}}$ , the  $u_c/U_\infty$  will recover almost in a linear fashion as  $s'$  increases. However, the trend is characterised by a slow recovery. In addition, it does not fully recover to the baseline level even at the largest  $s'$  investigated here.

In summary, Figure 4 provides a clear indication that both the LEBU<sub>2.5</sub> and LEBU<sub>5.0</sub> are capable of disrupting the turbulence convection, and very possibly also affecting the turbulence production downstream. The next section will focus on the wall pressure power spectral density subjected to LEBU.

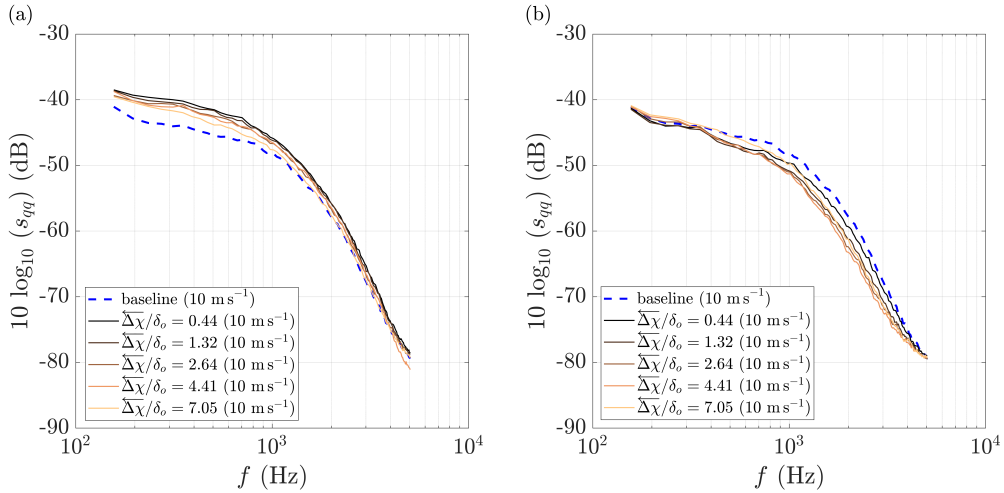


**Fig. 5** Fluctuating wall pressure spectra  $s_{qq}$  at  $\overrightarrow{\Delta x}/\delta_o = 3.52$  and  $U_\infty = 10 \text{ ms}^{-1}$  for (a) LEBU<sub>2.5</sub>, and (b) LEBU<sub>5.0</sub>.

## B. Wall pressure power spectral density

The analysis will now focus on the power spectral density of the wall pressure fluctuations,  $s_{qq}$ . Under a combination of different  $\overleftarrow{\Delta x}/\delta_o$ ,  $\overrightarrow{\Delta x}/\delta_o$ ,  $\tilde{h}$  and  $U_\infty$  in the test matrix, a very wide range of  $s_{qq}$  characteristics has been observed. Figure 5 shows two examples of the  $s_{qq}$  spectra at  $\overrightarrow{\Delta x}/\delta_o = 3.52$  and  $U_\infty = 10 \text{ ms}^{-1}$  for both the LEBU<sub>2.5</sub> and LEBU<sub>5.0</sub>. It is interesting, but perhaps not surprising to note that despite the utilisation of the same LEBU under a same flow condition, placing it at different  $\tilde{h}$  can produce significantly different unsteady wall pressure responses downstream. For example, the LEBU<sub>2.5</sub> shown in Figure 5(a) almost exclusively produces higher  $s_{qq}$  level, especially at low frequency, compared to its baseline counterpart, across the entire range of  $\overleftarrow{\Delta x}/\delta_o$  investigated here. However, if the LEBU is elevated from the wall surface, such as the LEBU<sub>5.0</sub> case in Figure 5(b), the entire range of  $\overleftarrow{\Delta x}/\delta_o$  will produce lower

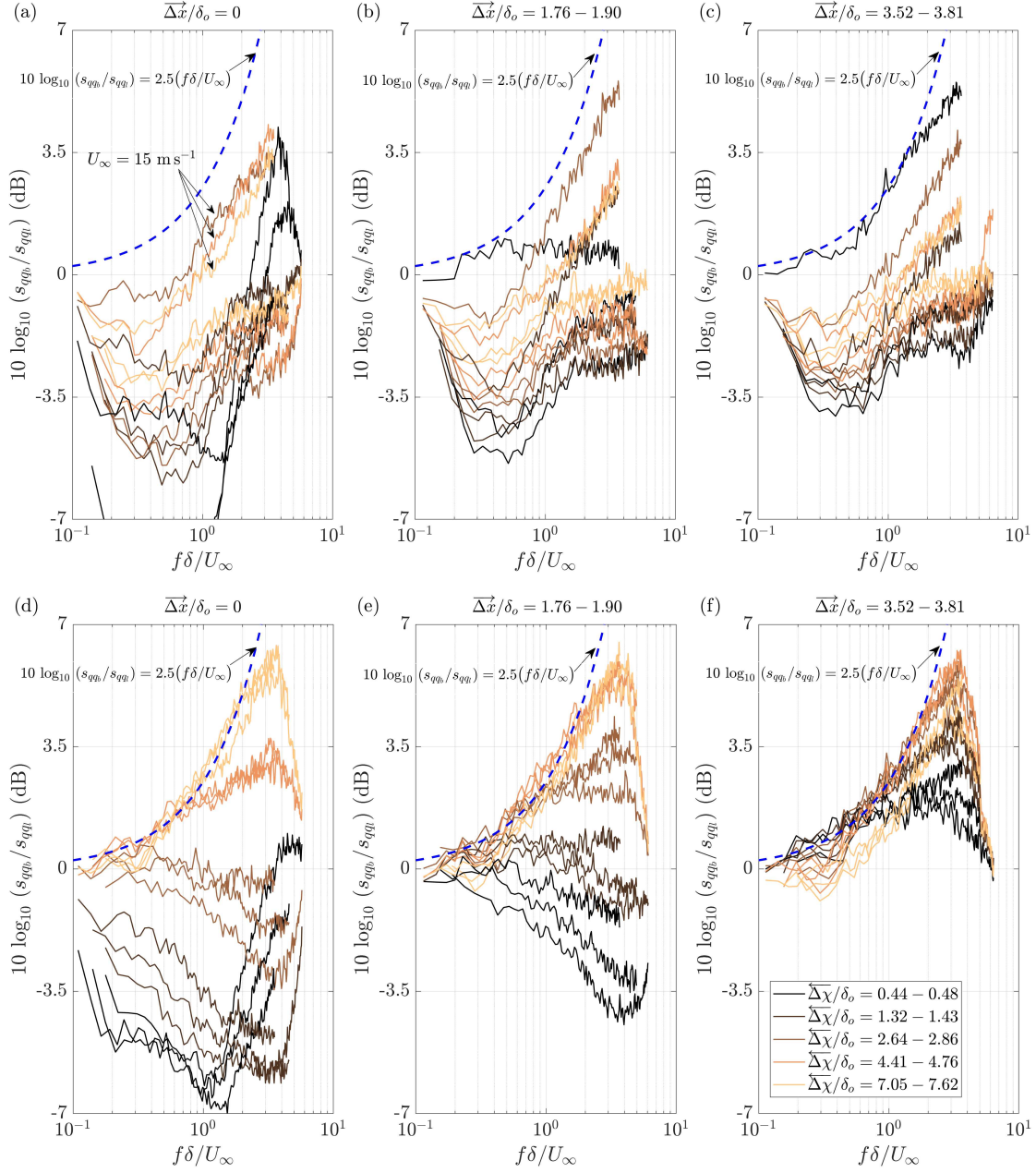


**Fig. 6**  $10 \log_{10}(s_{qqb}/s_{qqi})$  spectra measured across  $0.44 \leq \overline{\Delta x}/\delta_o \leq 7.62$  for (a-c) LEBU<sub>2.5</sub>, and (d-f) LEBU<sub>5.0</sub>. Each sub-figure contains spectra measured at  $U_\infty = 10, 12$  and  $15 \text{ m s}^{-1}$  across  $\overline{\Delta x}/\delta_o =$  (a, d) 0, (b, e) 1.76 – 1.90, and (c, f) 3.52 – 3.81.

level of  $s_{qq}$  across a large frequency range compared to the baseline.

To demonstrate all the results effectively, Figure 6 shows a summary of the difference in the fluctuating wall pressure spectra between the baseline,  $s_{qqb}$ , and those subjected to the LEBU,  $s_{qqi}$ , which are measured across combination of  $\overleftarrow{\Delta x}/\delta_o$ ,  $\overrightarrow{\Delta x}/\delta_o$ ,  $\tilde{h}$  and  $U_\infty$ . The frequency is non-dimensionalised by the local baseline boundary layer thickness  $\delta$  corresponding to the individual  $\overrightarrow{\Delta x}$  location, as well as the freestream velocity. A positive value of the  $10 \log_{10}(s_{qqb}/s_{qqi})$  denotes a reduction of wall pressure power spectral density level by the LEBU, and vice versa, when compared to the baseline level. Note that the variation of the  $10 \log_{10}(s_{qqb}/s_{qqi})$  is much more sensitive against the longitudinal separation distance between the LEBU and measurement point, than against the velocity. To make the comparison easier, for each combination of  $\overleftarrow{\Delta x}$  and  $\overrightarrow{\Delta x}$ , the wall pressure spectra at  $U_\infty = 10, 12$  and  $15 \text{ ms}^{-1}$  are bundled together in the same colour lines.

The analysis begins with Figure 6(a), which corresponds to the case of LEBU<sub>2.5</sub> and  $\overrightarrow{\Delta x}/\delta_o = 0$  (i.e.  $X_{\text{ref}}$ ). This sub-figure contains a collection of  $10 \log_{10}(s_{qqb}/s_{qqi})$  spectra pertaining to  $U_\infty = 10, 12$  and  $15 \text{ ms}^{-1}$ . With the LEBU<sub>2.5</sub> placing at  $0.44 \leq \overleftarrow{\Delta x}/\delta_o \leq 0.48$  (refer to sub-figure 6(f) for the legends), it is at a very close proximity to the surface microphone at  $\overrightarrow{\Delta x}/\delta_o = 0$ . This means that the microphone will be exposed to the direct impact from the emanated near wake. The effect is clearly manifested in the production of significant negative values of  $10 \log_{10}(s_{qqb}/s_{qqi})$  across the low frequency range, reaching a negative trough ( $\sim -10 \text{ dB}$ ) at  $f\delta/U_\infty \approx 0.5$ . However, as the frequency increases, the spectra exhibit a steep positive gradient, eventually reaching the positive level of  $10 \log_{10}(s_{qqb}/s_{qqi})$  at the higher frequency range. This phenomenon highlights the creation of highly non-equilibrium turbulent boundary layer under this particular LEBU treatment. Although not shown here, the decay rates of the wall pressure fluctuation spectra  $s_{qqi}$  for the LEBU are different from the baseline counterpart  $s_{qqb}$  across the entire frequency range. For example, the decay rate for the  $s_{qqi}$  at high frequency range is found to be  $\sim f^{-7}$ , which is significantly higher than the  $s_{qqb}$  counterpart that is characterised by  $\sim f^{-5}$  at the same frequency range. This indicates that the near wake produced by the LEBU<sub>2.5</sub> can cause a faster turbulent energy dissipation at the high frequency region. At  $U_\infty = 10$  and  $12 \text{ ms}^{-1}$ , the turbulent boundary layer will gradually return to its equilibrium state when  $\overleftarrow{\Delta x}/\delta_o$  increases, i.e. the LEBU<sub>2.5</sub> is shifted away from  $X_{\text{ref}}$  in the upstream direction, but the  $10 \log_{10}(s_{qqb}/s_{qqi})$  still remains predominantly negative across much of the frequency range. However, at  $U_\infty = 15 \text{ ms}^{-1}$ , there seems to be a deviation from the trend where the large scale turbulence structures at low frequency are perturbed less by the LEBU<sub>2.5</sub>. At high frequency, placing the LEBU<sub>2.5</sub> further upstream at  $\overleftarrow{\Delta x}/\delta_o \geq 2.8$  can even achieve significant positive level of  $10 \log_{10}(s_{qqb}/s_{qqi})$  ( $> 3.5 \text{ dB}$ ), i.e. reduction in the wall pressure power spectral density level compared to the baseline counterpart. In other words, the seemingly under-performing LEBU<sub>2.5</sub> could improve when the freestream velocity increases at large  $\overleftarrow{\Delta x}/\delta_o$ . This might be due to the turbulent boundary layer becoming thinner at higher  $U_\infty$ , causing the LEBU<sub>2.5</sub> to encounter larger effective  $\tilde{h}u_\tau/\nu$  locally. As a result, the LEBU<sub>2.5</sub> is increasingly situated near the outer layer. This highlights the importance to utilise LEBU effectively to target the large scale turbulence structures that are more dominant at the outer layer.

Within the same range of  $\overleftarrow{\Delta x}/\delta_o$ , it will be of interest to examine the effects of LEBU<sub>2.5</sub> on the fluctuating wall pressure at downstream locations (i.e.  $\overrightarrow{\Delta x}/\delta_o > 0$ ). Figure 6(b) and 6(c) show the  $10 \log_{10}(s_{qqb}/s_{qqi})$  spectra at  $\overrightarrow{\Delta x}/\delta_o = 1.76 - 1.90$ , and  $3.52 - 3.81$ , respectively. At  $U_\infty = 10$  and  $12 \text{ ms}^{-1}$ , the trend of  $10 \log_{10}(s_{qqb}/s_{qqi})$  is still predominantly of negative level at the low frequency, but it will gradually recover as the  $\overrightarrow{\Delta x}/\delta_o$  increases. The same trend is also observed for the high frequency range where the magnitude of  $10 \log_{10}(s_{qqb}/s_{qqi})$  becomes closer to the zero datum, i.e. conforming to the baseline level. At  $U_\infty = 15 \text{ ms}^{-1}$  and  $\overrightarrow{\Delta x}/\delta_o = 1.76 - 1.90$ , and  $3.52 - 3.81$ , the LEBU<sub>2.5</sub> follows the same trend we had observed earlier at  $\overrightarrow{\Delta x}/\delta_o = 0$  and continues to produce positive values of  $10 \log_{10}(s_{qqb}/s_{qqi})$  spectra at the mid and high frequencies. Interestingly, the optimal LEBU location has been shifted from  $\overleftarrow{\Delta x}/\delta_o > 2.8$  at  $\overrightarrow{\Delta x}/\delta_o = 0$  to  $\overleftarrow{\Delta x}/\delta_o \approx 0.5$  at  $\overrightarrow{\Delta x}/\delta_o = 3.7$ . Therefore, the optimal distance between the LEBU's trailing edge and the targeted wall pressure location should fall within  $2.8 < s' (= \overleftarrow{\Delta x}/\delta_o + \overrightarrow{\Delta x}/\delta_o) < 4.2$  for this particular case. This condition suggests that an optimal value of  $s'$  exists for the mitigation of the wall pressure fluctuations.

Next, the  $10 \log_{10}(s_{qqb}/s_{qqi})$  spectra subjected to the LEBU<sub>5.0</sub> as a function of  $\overleftarrow{\Delta x}/\delta_o$ ,  $\overrightarrow{\Delta x}/\delta_o$  and  $U_\infty$  are shown in Figure 6(d–f). The LEBU<sub>5.0</sub> is found to be more effective for the mitigation of wall pressure fluctuations, and more importantly many of the  $10 \log_{10}(s_{qqb}/s_{qqi})$  spectra it produces seem to follow a self-similar behaviour. The following bullet points summarise the observations so far for the LEBU<sub>5.0</sub> case:

- assuming a scenario whereby the trailing edge of the LEBU<sub>5.0</sub> is situated at  $\overleftarrow{\Delta x}/\delta_o = 0$ , i.e. at exactly the same streamwise location as  $\overrightarrow{\Delta x}/\delta_o = 0$ , the corresponding vertical distance in wall unit is  $\tilde{h}u_\tau/\nu \approx 170 - 240$ . By traversing the LEBU<sub>5.0</sub> towards the upstream direction from  $\overleftarrow{\Delta x}/\delta_o = 0.44$  to  $7.62$ , the  $\tilde{h}u_\tau/\nu$  encountered by the LEBU<sub>5.0</sub> trailing edge will continue to increase. This ensures that the LEBU<sub>5.0</sub> will always remain as a source targeting device for the outer part of turbulent boundary layer.
- the effectiveness of LEBU<sub>5.0</sub> in the mitigation of the wall pressure fluctuations is highly dependent on the  $\overleftarrow{\Delta x}/\delta_o$ . Based on the results in Figure 6(d–f), it is found that the  $10 \log_{10}(s_{qqb}/s_{qqi})$  will only become positive when  $s' > 3$ . This is an important observation that will be discussed further.
- the normalised frequency corresponding to the maximum wall pressure reduction always occurs at  $f\delta/U_\infty = 3.5$ .
- the variation of  $10 \log_{10}(s_{qqb}/s_{qqi})$  against the frequency is found to follow closely  $2.5(f\delta/U_\infty)$ , as shown in the figure. This represents the upper limit on the wall fluctuating pressure reductions by this particular type of LEBU. Interestingly, this limiting curve also applies to the LEBU<sub>2.5</sub> case, as shown in Figure 6(a–c).

Following the discussion of the spectral characteristics, the next step is to examine the *overall* wall pressure fluctuations  $S_{qqi}$  subjected to the LEBU treatment. The  $S_{qqi}$ , which is obtained by integrating the wall pressure fluctuation  $\int_f s_{qqi} df$  between 0.15 and 6 kHz, will be close to the standard deviation of the wall pressure fluctuations. Figure 7(a, b) show the variations of  $10 \log_{10}(S_{qqb}/S_{qqi})$  against  $s'$  at several targeting locations under a range of

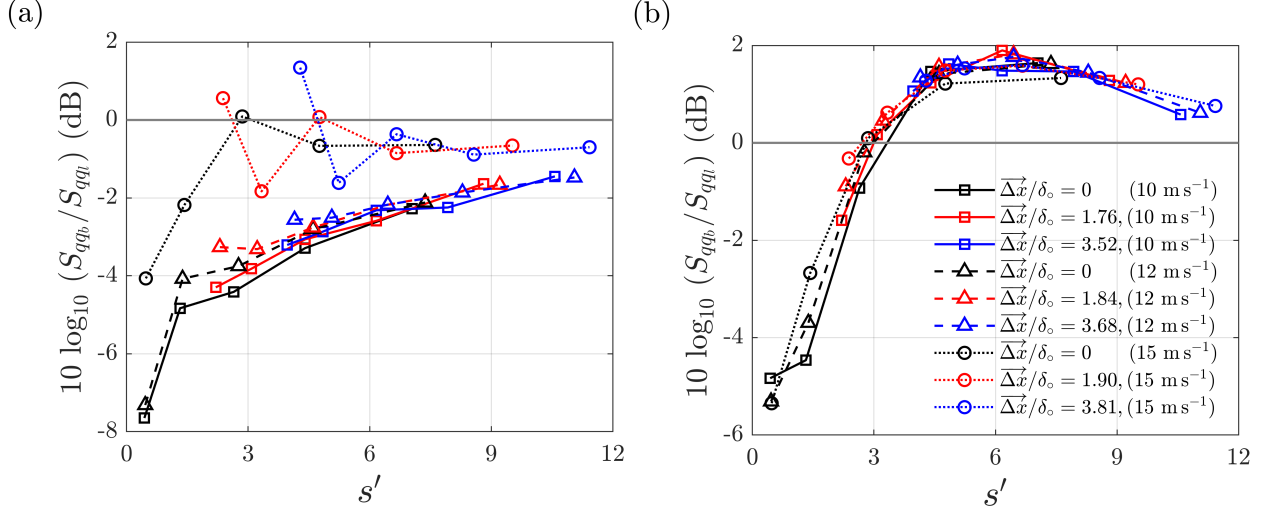


**Fig. 7** Difference in the overall fluctuating wall pressure,  $10 \log_{10}(S_{qqb}/S_{qqi})$ , against  $s'$  for (a) LEBU<sub>2.5</sub>, and (b) LEBU<sub>5.0</sub>.

freestream velocity. Note that the  $S_{qqb}$  represents the overall wall pressure fluctuations for the baseline case. Generally, the trends are very similar to the spectra discussed earlier. The ineffectiveness of the LEBU<sub>2.5</sub> in mitigating the wall pressure fluctuation is again manifested in Figure 7(a) where negative values of  $10 \log_{10}(S_{qqb}/S_{qqi})$  are dominant. The curves collapse for both the  $U_{\infty} = 10$  and  $12 \text{ m s}^{-1}$  cases, where an initial detrimental outcome at low  $s'$  will gradually abate as the normalised separation distance between the LEBU and the targeting location increases. However, at  $U_{\infty} = 15 \text{ m s}^{-1}$ , where in previous analysis had indicated that the LEBU<sub>2.5</sub> is approaching the outer part of the turbulent boundary layer, deviation from the trend becomes obvious and the wall pressure fluctuations are now closer to the baseline level.

An important result of this study is featured in Figure 7(b), where a high level of self-similar behaviour is achieved by the LEBU<sub>5.0</sub> case throughout the ranges of normalised targeting location and freestream velocity investigated here. The onset of reduction for the overall wall pressure fluctuations is found to occur at  $s' = 3$ . The maximum reduction occurs at  $s' = 6$ . After that, the level of reduction will start to fall. Both the  $s'$  and wake emanated from the LEBU have important roles in establishing the self-similar behaviour of the wall pressure spectrum. Placing the LEBU<sub>5.0</sub> too close to the measurement point, i.e.  $s' < 3$ , where the wake emanated from the LEBU is still relatively narrow, will actually enhance the low frequency wall pressure fluctuation. The enhancement across the low and high frequencies wall pressure fluctuations can be attributed to the overall increase of turbulence intensity across the non-equilibrium turbulent boundary layer [11]. On the other hand, at larger  $s'$ , the LEBU wake would have developed quite considerably such that the entire turbulence self-sustaining mechanism (e.g. the burst and sweep events) are severely disrupted, which is manifested in the significant reduction of turbulence intensity across the turbulent boundary layer [11].

Although the range of  $\tilde{h}$  investigated here is not exhaustive, these non-dimensional values could represent a simple LEBU's optimisation rule in the mitigation of wall pressure fluctuations at zero pressure gradient flow.

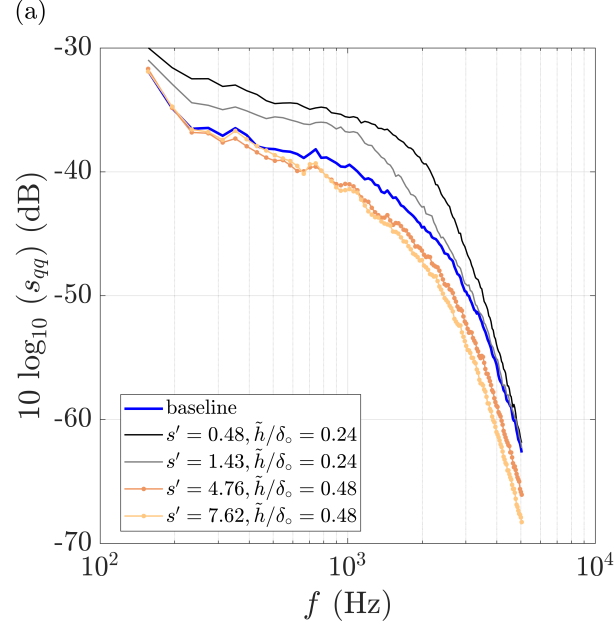


**Fig. 8** Fluctuating wall pressure spectra  $s_{qq}$  for the baseline and different combinations of  $s'$  and  $\tilde{h}/\delta_o$ .  $\delta_o$  is the turbulent boundary layer thickness at  $X_{\text{ref}}$ .

### C. Boundary layer analysis of LEBU at different $\tilde{h}$ and $s'$

Turbulent spots are widely recognised as the building blocks of turbulent boundary layers. Studying their spatio-temporal evolution offers a unique and effective way to gain fundamental insights into the generation mechanisms of turbulent wall pressure sources [11]. This approach can be applied to examine the interaction between turbulent spots and LEBU wakes with varying  $\tilde{h}$  and  $s'$ . In this study, turbulent spots were triggered near the flat plate's leading edge in a controlled manner, allowing them to propagate downstream and encounter the LEBU wake along the way.

For brevity, the instrumentation, method of generating turbulent spots and data analysis technique will not be repeated here, but readers can refer to Chong and Muhammad [11] for detailed information.

Figure 8 presents a selection of wall pressure fluctuation spectra produced by the configuration shown in Figure 1, where a boundary layer trip tape is used. The spectra in Figure 8 can be divided into three categories. The first represents the baseline. The second corresponds to cases when the LEBU is positioned relatively close to both  $X_{\text{ref}}$  and the wall surface, with  $s' < 3$  and  $\tilde{h}/\delta_o < 0.3$ . In this category, the resulting wall pressure spectra are more detrimental compared to the baseline. The third category pertains to configurations where the LEBU is placed farther from both  $X_{\text{ref}}$  and the wall surface, with  $s' > 3$  and  $\tilde{h}/\delta_o > 0.3$ . In this case, the wall pressure spectra are lower than the baseline across almost the entire frequency range, as shown in Figure 8.

When the boundary layer trip tape is removed and turbulent spots are triggered [11], Figure 9 presents contour maps of velocity perturbation,  $\tilde{u}(y/\delta_{\text{spot}}, t')$ , corresponding to the three categories previously described. Here,  $\delta_{\text{spot}}$  represents the maximum boundary layer thickness of the turbulent spot at  $X_{\text{ref}}$ , and  $t'$  is the non-dimensional time of flight of

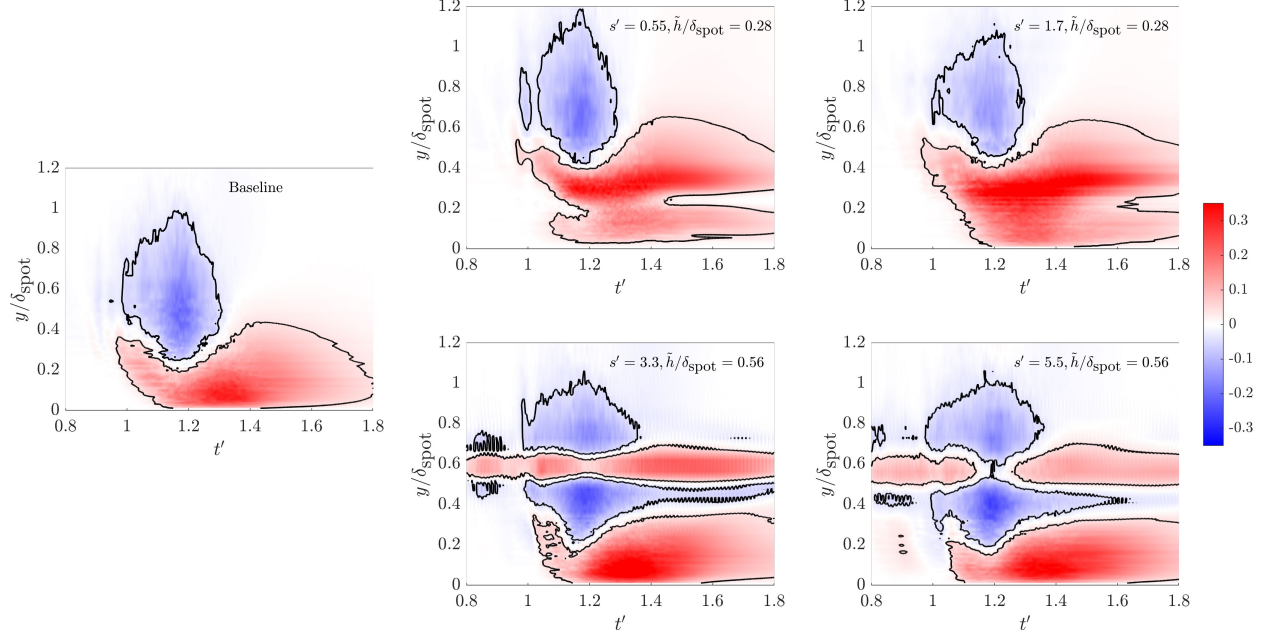


**Fig. 9** Contour maps of the velocity perturbations  $\tilde{u}(y/\delta_{\text{spot}}, t')$  for the **Category 1 (baseline)**, **Category 2** ( $y/\delta_{\text{spot}} < 0.30$  and  $s' < 3$ ) and **Category 3** ( $y/\delta_{\text{spot}} > 0.30$  and  $s' > 3$ ).

the turbulent spot, with  $t' = 1$  indicating its arrival at  $X_{\text{ref}}$  after being triggered at  $t' = 0$ . The velocity perturbation,  $\tilde{u}$ , reflects the momentum exchange due to turbulent flow. For reference, contour lines of  $\tilde{u} = \pm 0.04$  are superimposed to outline the overall shape of the turbulent spots. The ensemble-averaged spot reveals four key regions: (1) near-wall positive perturbations, (2) outer-layer negative perturbations. Both features of (1) and (2) reflect a typical turbulent boundary layer velocity profile; (3) a leading edge overhang from ejected turbulent fluid that decays outside the boundary layer, and (4) a becalmed region behind the spot formed by downstream sweeping of high-momentum fluid. This region has a more stable velocity profile than the laminar boundary layer. The overall contour matches findings in the literature [16–18].

The analysis then shifts to the second category. Here, the LEBU wake, generated at  $y/\delta_{\text{spot}} = 0.28$  with  $s' < 3$ , causes the entire turbulent spot to lift away from the wall surface. Despite this spatial displacement, the overall shape and internal momentum distribution of the turbulent spot remain largely unchanged. This indicates that the turbulent fluid’s momentum transport is unaffected, suggesting minimal impact on wall pressure fluctuations. However, the clear presence of a high-momentum LEBU wake, as evidenced by the positive  $\tilde{u}$  streak beneath the turbulent spot and close to the wall surface, acts as an additional source of turbulent wall pressure. This explains the observed increase in wall pressure fluctuations, as shown in Figure 8.

When the LEBU wake is generated at  $y/\delta_{\text{spot}} = 0.56$  with  $s' > 3$ , it falls into the third category, where the velocity contour maps no longer display any “lift-up” effect on the turbulent spot. Instead, the LEBU wake penetrates the outer-layer negative perturbation region, effectively bisecting the turbulent spot into two parts. Additionally, the LEBU

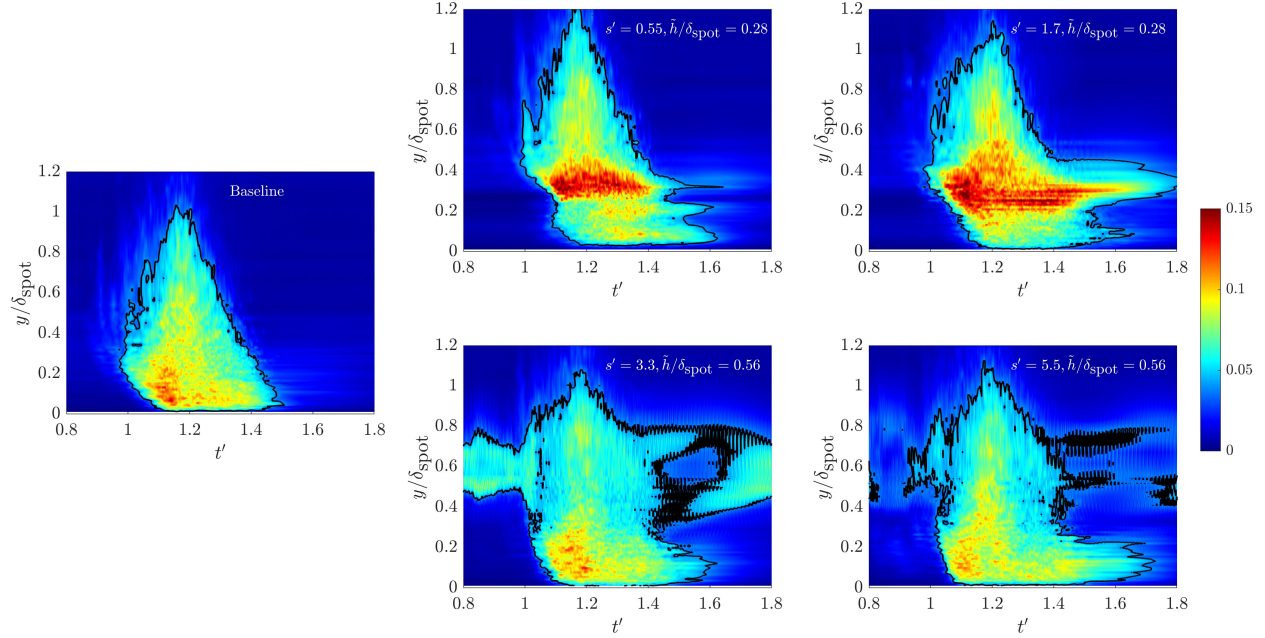


**Fig. 10** Contour maps of the velocity fluctuations  $u'(y/\delta_{\text{spot}}, t')$  for the Category 1 (baseline), Category 2 ( $y/\delta_{\text{spot}} < 0.30$  and  $s' < 3$ ) and Category 3 ( $y/\delta_{\text{spot}} > 0.30$  and  $s' > 3$ ).

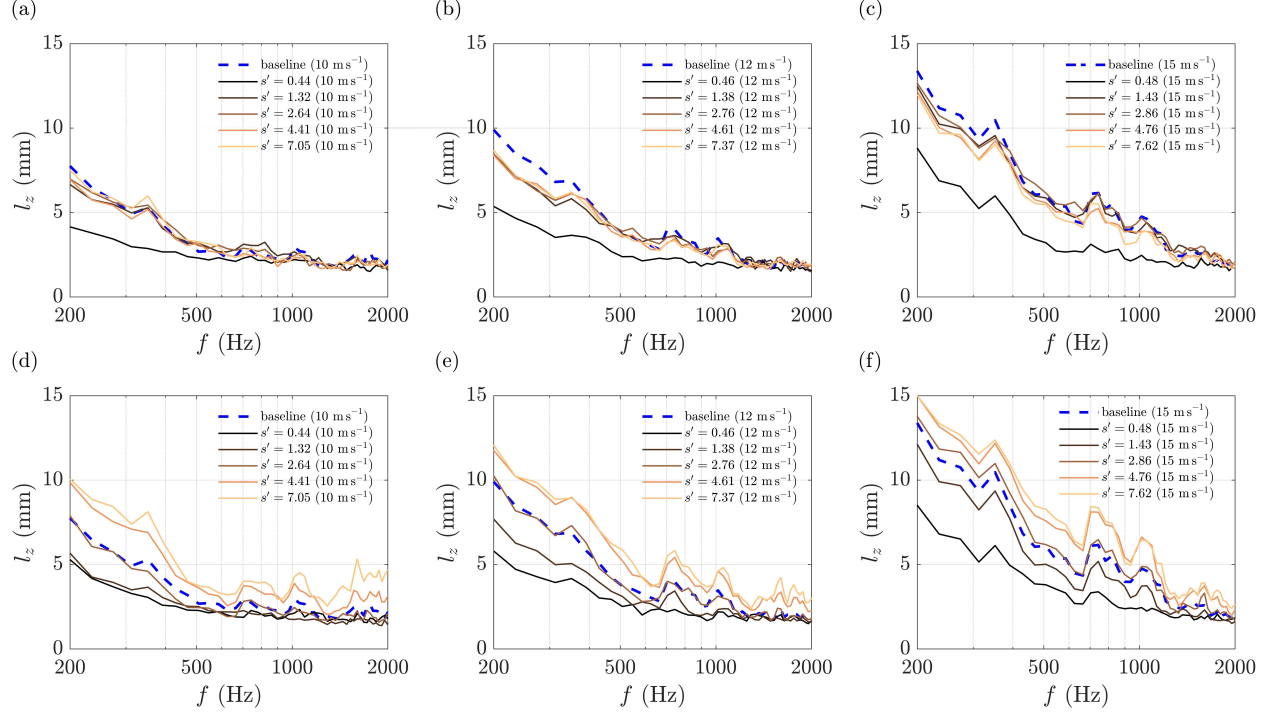
wake exhibits significant oscillatory behavior, which not only alters the turbulent fluid mixing and entrainment processes but also disrupts the turbulence regeneration mechanism. For further analysis of the impact of LEBU wake oscillation in the outer layer, see Chong and Muhammad [11]. However, in the context of the current study, the consequence of such disruption is readily demonstrated by the turbulent velocity.

Figure 10 presents contour maps of velocity fluctuation,  $u'(y/\delta_{\text{spot}}, t')$ , for the same three categories. The baseline turbulent spot, defined by turbulence intensity, differs from that defined by velocity perturbation, but key features like the leading edge overhang, and trailing edge remain distinct. The becalmed region diminishes due to low turbulence intensity. Near the wall, the leading edge and area under the overhang exhibit high turbulence intensity (10 – 14%), termed “primary turbulence intensity,” which destabilises the surrounding laminar layer. This is consistent with previous observations of turbulence production at the leading edge. A “secondary turbulence intensity” (8 – 10%) surrounds regions linked to the negative (outer layer) and positive (inner layer) perturbations.

In the second category, where the LEBU wake was generated at  $y/\delta_{\text{spot}} = 0.28$  and  $s' < 3$ , turbulence levels are elevated in both the primary and secondary intensity regions, which are also displaced upward by the LEBU wake. This increase is due to mixing between the turbulence and the incoming wake. Additionally, a strong turbulence regime forms beneath the shifted turbulent spot. Integration of  $u'$  across the spatial and temporal domains shows that the overall turbulence energy is higher than in the baseline case.

For the third category, where the LEBU wake was generated at  $y/\delta_{\text{spot}} = 0.56$  and  $s' > 3$ , the turbulence distribution closely aligns with its perturbation counterpart. The LEBU wake penetrates the outer layer, effectively isolating it from

the inner layer and disrupting the ejection and sweeping mechanisms necessary for sustaining the turbulent boundary layer's growth. This results in a lower turbulence intensity across most of the turbulent spot compared to the baseline. Consequently, the reduced turbulence levels lead to decreased wall pressure fluctuations, as shown in Figure 8.



**Fig. 11** Lateral coherence length spectra  $l_z(f)$  for different  $s'$  at  $U_\infty =$  (a, d)  $10 \text{ ms}^{-1}$ , (b, e)  $12 \text{ ms}^{-1}$  and (c, f)  $15 \text{ ms}^{-1}$  for (a–c) LEBU<sub>2.5</sub> and (d–f) LEBU<sub>5.0</sub>.

#### D. Lateral turbulence length scales

After the study of turbulent spots in the previous section, the analysis now returns to the two-dimensional turbulent boundary layer generated by the trip tape as per the configuration in Figure 1. The lateral (spanwise) coherence function of two microphone signals,  $\gamma_z^2$ , can describe a turbulence structure and its physical size in the frequency domain.

$$\gamma_z^2(f) = \frac{|\Phi_{z_i z_j}(f)|^2}{\Phi_{z_i z_i}(f) \Phi_{z_j z_j}(f)}. \quad (1)$$

In the equation,  $\Phi_{z_i z_j}(f)$  is the cross power spectral density between two wall pressure fluctuating signals at locations  $z_i$  and  $z_j$ . The wall pressure signal at  $z_i$  is usually designated as the reference microphone sensor located at  $\vec{\Delta x}/\delta_o = 0$  ( $X_{\text{ref}}$ ), which is also at the mid-span ( $z = 0$ ) of the flat plate. Therefore,  $\Phi_{z_i z_i}(f)$  and  $\Phi_{z_j z_j}(f)$  are the auto power spectral density for the reference ( $i$ ) and  $j^{\text{th}}$  wall pressure fluctuations, respectively.

$$l_z(f) = \int_0^\infty \sqrt{\gamma_z^2(z, f)} dz. \quad (2)$$

As shown in Equation 2, an integration of the spanwise coherence magnitude across the lateral location can result in the lateral coherence length of the turbulence,  $l_z$ , as a function of frequency.  $l_z$  is one of the important turbulent sources for the trailing edge noise radiation [3]. In the current work, a total of seven different  $\Delta z$  are used for the calculation of the  $l_z$ . This sub-section will study the responses of  $l_z$  subjected to both the LEBU<sub>2.5</sub> and LEBU<sub>5.0</sub> under different  $\overleftarrow{\Delta x}/\delta_o$  and  $U_\infty$ , but only at  $\overrightarrow{\Delta x}/\delta_o = 0$  ( $X_{\text{ref}}$ ). Therefore, from hereon, and also remainder of the paper, the expression of the normalised streamwise separation distance between the LEBU and target location is solely described by the  $s'$ .

Figure 11 shows the spectra of lateral coherence length  $l_z$  for both the LEBU<sub>2.5</sub> and LEBU<sub>5.0</sub> at  $10 \leq U_\infty \leq 15 \text{ ms}^{-1}$ . For the LEBU<sub>2.5</sub> case, there is a clear reduction of  $l_z$  against the baseline when it is placed close to the  $X_{\text{ref}}$  where  $s' < 0.44 - 0.48$ . When the  $s'$  increases, the differences in  $l_z$  against the baseline become smaller, but majority of them still exhibit lower levels. Therefore, as far as the lateral turbulence coherence length scale is concerned, the LEBU<sub>2.5</sub> is favourable for achieving low-noise aeroacoustics. Interestingly, this characteristic is completely contradictory to the wall pressure fluctuations where majority of them exhibit increase of magnitude against the baseline (see Figure 6a).

For the LEBU<sub>5.0</sub>, placing it at close proximity to the  $X_{\text{ref}}$ , i.e.  $s' < 0.44 - 0.48$  would repeat the previous trend where a significant reduction in the lateral coherence length is achieved across a large frequency range. However, at the larger  $s'$  distance, instead of conforming to the baseline level, the lateral coherence length continues to increase, even surpassing the baseline level when  $s' > 3$ . This characteristic is again completely opposite to the wall pressure fluctuation counterparts, as shown in Figure 6(d).

### E. Implication to the self-noise radiation subjected to LEBU

A trend now emerges that when a LEBU is placed at  $s' < 3$ , the intense interaction between the local turbulent boundary layer and the emanated near wake will enhance the wall pressure fluctuation, but weaken the lateral coherence length of the turbulence. The opposite can be said true, especially for the LEBU<sub>5.0</sub> case. When it is displaced further upstream from the targeted location, reduction of the wall pressure fluctuations against the baseline can be realised, but this comes at the expense of larger lateral coherence length of turbulence to be produced. How the aeroacoustics properties responding to these contradictory behaviours represent the focus of this section.

The relationship between the far field pressure (i.e. noise) and the near field wall pressure fluctuation near the trailing edge of an aerofoil is made explicitly in the classical work of [3], who derived a direct relationship between the power spectral density of the far field trailing edge noise ( $s_{pp}$ ) of an aerofoil for an observer in the centre-line plane of an aerofoil with span  $2d$ , chord,  $2b$ , to the wall pressure spectra ( $s_{qq}$ ) by:

$$s_{pp}(x, 0, y, \omega) = \left( \frac{\omega by}{2\pi c_o \sigma^2} \right)^2 d |\mathfrak{Q}|^2 l_z(\omega) s_{qq}(0, \omega), \quad (3)$$

where  $\omega$  is the angular frequency,  $\sigma^2$  is a Mach number corrected geometrical function, and  $|\mathfrak{Q}|$  is the norm of the

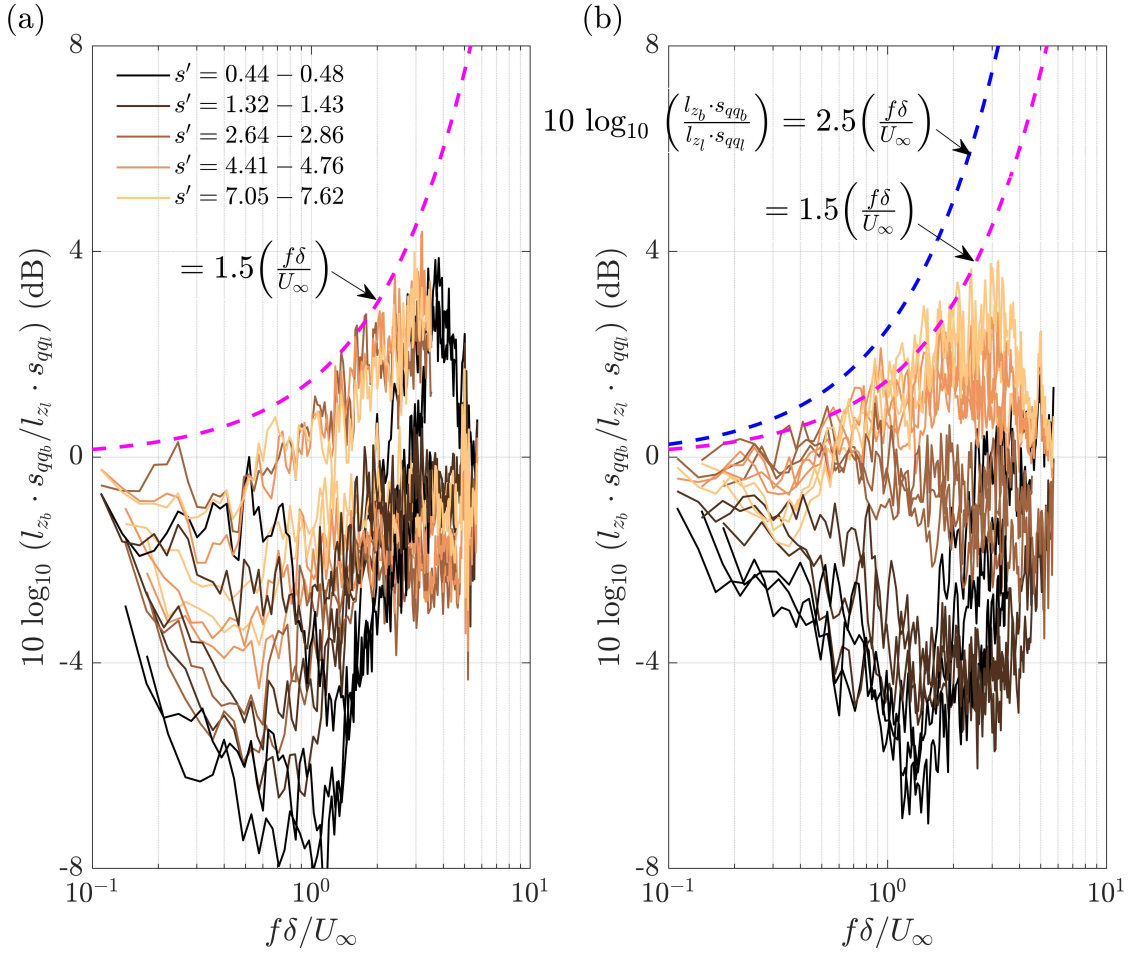


**Fig. 12** Difference in the Amiet noise source  $10 \log_{10}(l_{z_b} \cdot s_{qq_b} / l_{z_l} \cdot s_{qq_l})$  for different  $s'$  by (a)  $LEBU_{2.5}$ , and (b)  $LEBU_{5.0}$ . Both sub-figures contain spectra measured at  $U_{\infty} = 10, 12$  and  $15 \text{ ms}^{-1}$ .

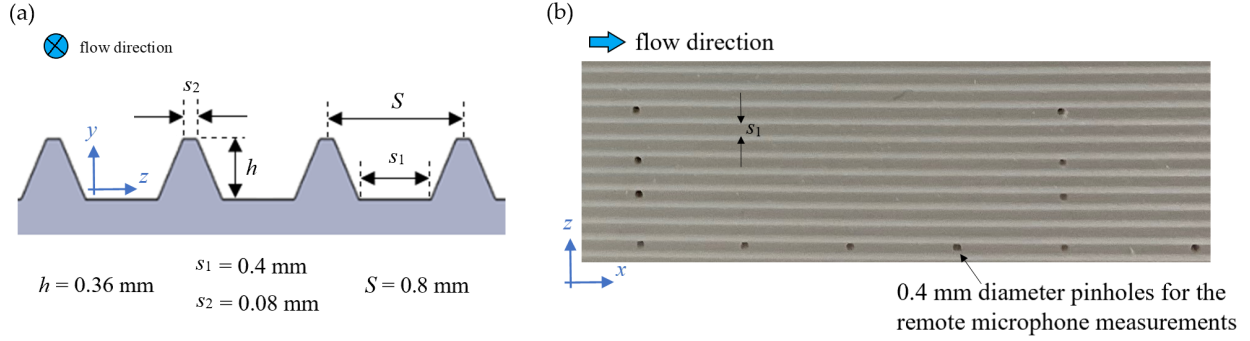
acoustical transfer function. From Equation 3, the product of the lateral coherence length ( $l_z$ ) and wall pressure spectra ( $s_{qq}$ ) represents the main combined sources of the radiated spectrum ( $s_{pp}$ ). Although no aeroacoustics measurement on aerofoil is performed in this study, it might still be possible to evaluate the effect of LEBU on the trailing edge noise radiation by examining the  $10 \log_{10}(l_z \cdot s_{qq})$ . Note that the analysis does not consider the self-noise generated by the LEBU.

Figure 12(a–b) show the spectra of  $10 \log_{10}(l_{z_b} \cdot s_{qq_b}/l_{z_l} \cdot s_{qq_l})$ , as a function of the normalised frequency, for both the LEBU<sub>2.5</sub> and LEBU<sub>5.0</sub>. The subscripts “b” and “l” represent the baseline and LEBU, respectively. A positive value denotes reduction of the Amiet noise sources against the baseline, and vice versa. The minima and maxima of the Amiet noise sources subjected to the LEBU<sub>2.5</sub> in Figure 12(a) largely occur at the same non-dimensional frequencies as the wall pressure fluctuations in Figure 6(a). However, the Amiet noise sources spectra would exhibit a better self-similar behaviour than the wall pressure fluctuation spectra. The spectra are bounded by an upper limiting line of the Amiet noise source at  $1.5(f\delta/U_\infty)$ . An interesting observation from Figure 12(a) is that, at  $s' > 2.64$ , all the spectra produced at  $U_\infty = 15 \text{ ms}^{-1}$  are close to the limiting line. As discussed earlier, the LEBU<sub>2.5</sub> will entail a larger value of  $\tilde{h}u_\tau/\nu$  at higher freestream velocity such that it is increasingly targeting the large scale structure at the outer layer to reap the benefits of turbulent wall pressure reductions. In Figure 12(b) for the LEBU<sub>5.0</sub>, the upper limit of the Amiet noise sources reduction is also found to fit better to  $1.5(f\delta/U_\infty)$ , instead of the  $2.5(f\delta/U_\infty)$  pertaining to the upper limit for the wall pressure fluctuations as depicted in Figure 6(d–f). This phenomenon is a manifestation of the counter-balancing effect between the wall pressure fluctuation and turbulence lateral coherence length.

Although the LEBU<sub>2.5</sub> is not as effective as the LEBU<sub>5.0</sub> in the suppression of the Amiet noise sources, a number of common characteristics between them can still be extracted from Figure 12(a–b). First, the minima and maxima of the  $10 \log_{10}(l_{z_b} \cdot s_{qq_b}/l_{z_l} \cdot s_{qq_l})$  occur at  $f\delta/U_\infty \approx 1$  and  $3.5$ , respectively. Second, the upper limit of the Amiet noise sources reduction,  $1.5(f\delta/U_\infty)$ , is applicable to both cases. Third, reduction of the Amiet noise sources is not possible at the low frequency, typically at  $f\delta/U_\infty < 0.3$ . This represents the limitation of LEBU in tackling the low frequency noise source.

#### IV. Simultaneous application of Riblets and LEBU (RIBU)

Using the same experimental setup and analysis techniques as the current one, we have observed that targeting the near wall turbulence by the riblets can reduce the Amiet noise sources at low and high frequencies, but exhibit no effect at the mid frequency region [6]. The different frequency responses of  $10 \log_{10}(l_{z_b} \cdot s_{qq_b}/l_{z_l} \cdot s_{qq_l})$  produced by the riblets and LEBU, respectively, raise a research question of whether they can complement each other, in the form of RIBU, to jointly mitigate the overall Amiet noise sources. Although a comprehensive investigation of this research topic is beyond the current scope, some preliminary investigations of the RIBU have been conducted and the results are presented here.



**Fig. 13** (a) Front view illustrating the riblets geometry, and (b) plan view showing a zoomed-in view of the riblets test plate. Reprinted from “Mitigation of turbulent noise sources by riblets” by Muhammad and Chong, 2022, *Journal of Sound and Vibration* 541, 117302, with permission from Elsevier.

### A. Design of the riblets plate

All the results presented thus far, where only the LEBU is utilised, are subjected to a smooth surface at the interchangeable test plate shown in Figure 1. To investigate the “RIBU”, the interchangeable test plate will be replaced with a riblets type. The riblets test plate is manufactured in-house by a Stereolithography Apparatus (SLA) 3D printing technique. Figure 13 summarises the riblets configuration and dimensions, whose shape can be characterised by a simple longitudinal sawtooth with a flat surface between each protuberance.

The riblets geometry can be described by  $h$ ,  $s_1$ ,  $s_2$  and  $S$ . The  $s_1$  is pre-determined as 0.4 mm to correspond to the pressure tap hole diameter. The  $s_2$ , which is ideally  $\rightarrow 0$ , is estimated to be 0.08 mm, which is equivalent to the laser beam diameter used in the 3D printing. The friction velocities  $u_\tau$  are determined from the measured boundary layer profiles to non-dimensionalise the riblets’ height ( $h^+ = hu_\tau/\nu$ ) and lateral spacing between protuberance ( $S^+ = Su_\tau/\nu$ ). The riblets achieve  $h^+ = 12.2, 14.3$  and  $17.4$  at  $U_\infty = 10, 12$  and  $15$   $\text{ms}^{-1}$ , respectively. Therefore, the riblets are expected to fall within the buffer region of a turbulent boundary layer and confirm its status as an inner layer flow control device. For the lateral spacing,  $S^+$  equals to 27.1, 31.9 and 38.7 at  $U_\infty = 10, 12$  and  $15$   $\text{ms}^{-1}$ , respectively. These values suggest that, despite the application of spanwise offset to each of the riblets protuberance ( $s_1$ ), they are still significantly smaller than the mean lateral spacing between adjacent low-speed streaks of the coherent structures whose  $\Delta z^+ = \Delta zu_\tau/\nu \sim 100$ . The riblets depicted in Figure 13 is indeed effective in the manipulation of zero pressure gradient turbulent boundary layer, as demonstrated in Muhammad and Chong [6].

Note that the spanwise distribution of the pressures tab for the riblets test plate can be slightly different compared to the values of the smooth flat plate. This is due to the adjustment of the pressure tab to ensure that it is located within the valley of each groove of the riblets. Nevertheless, the difference is very small ( $\leq 0.3$  mm), thus can be treated as negligible.

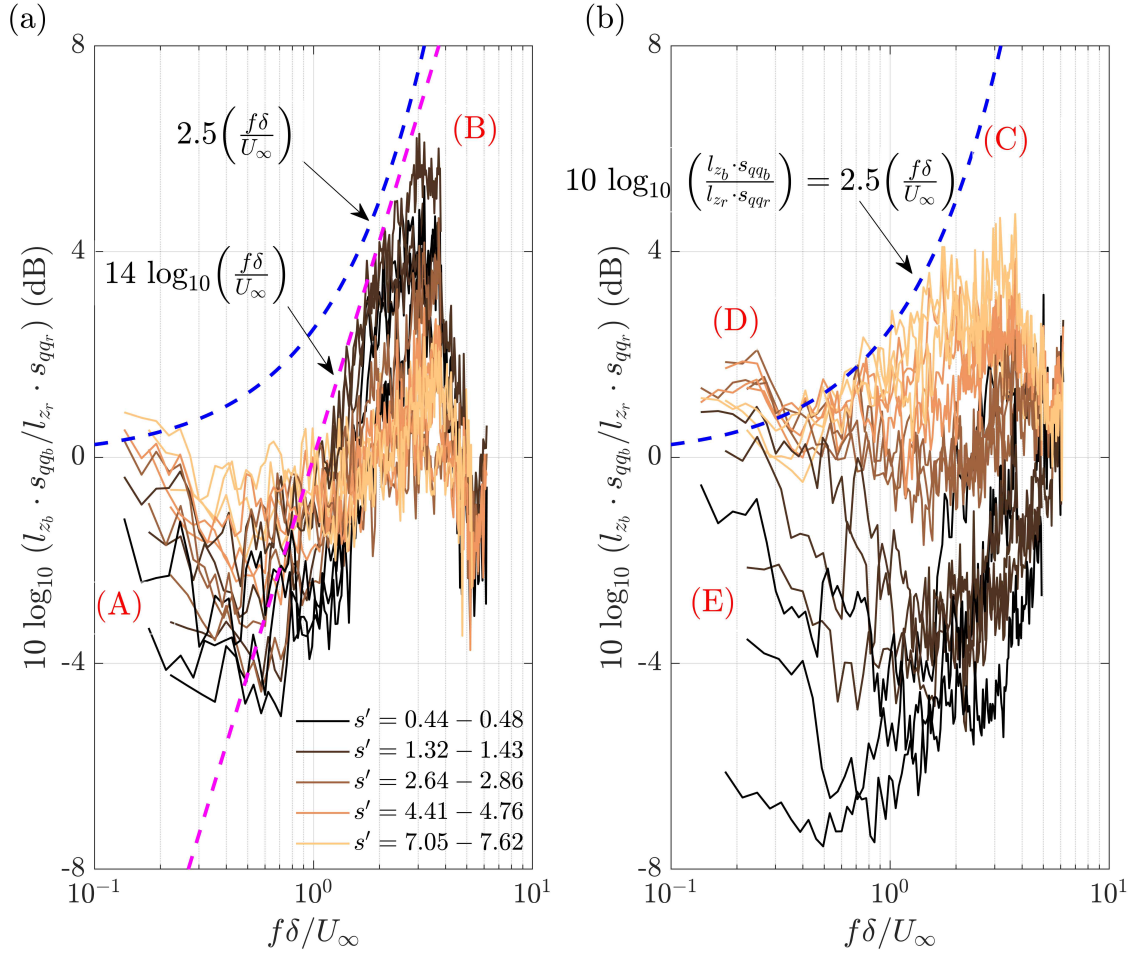


**Fig. 14** Difference in the Amiet noise source  $10 \log_{10}(l_{z_b} \cdot s_{qq_b} / l_{z_r} \cdot s_{qq_r})$  for different  $s'$  by (a) riblets + LEBU<sub>2.5</sub>, and (b) riblets + LEBU<sub>5.0</sub>. Both sub-figures contain spectra measured at  $U_\infty = 10, 12$  and  $15 \text{ ms}^{-1}$ .

## B. Implication to the self-noise radiation subjected to RIBU

Using the exact same LEBU configurations and  $s'$  range that produced the Amiet noise source spectra in Figure 12(a–b), but with the addition of riblets whose configuration has been briefly described in Section IV.A, Figure 14(a–b) shows the  $10 \log_{10}(l_{z_b} \cdot s_{qq_b}/l_{z_r} \cdot s_{qq_r})$  spectra for the RIBU cases. Note that  $l_{z_r}$  and  $s_{qq_r}$  are the spanwise turbulence coherence length and wall pressure fluctuations, respectively, subjected to the RIBU treatment. The coverage of the riblets is  $500 \leq x \leq 749$  mm, whereas the placements of the LEBU encompass  $545 \leq x \leq 620$  mm (see Table 1). The followings summarise five major characteristics of the RIBU, which can be cross-referenced to the annotations in the figure:

- (A) The abilities of the riblets to reduce both the lateral turbulence coherence length and wall pressure fluctuations at low frequency, which have been demonstrated in [6], seem to transfer to the RIBU in such a way that the enhancement of the Amiet noise sources at low frequency by the LEBU<sub>2.5</sub> (see Figure 12a) can be mitigated effectively by the addition of the riblets. The reduced minima of the  $10 \log_{10}(l_{z_b} \cdot s_{qq_b}/l_{z_r} \cdot s_{qq_r})$  also appear to be shifted from  $f\delta/U_\infty = 1$  to  $f\delta/U_\infty = 0.6$ .
- (B) The addition of riblets in conjunction with the LEBU<sub>2.5</sub> has a significant impact on the maxima of  $10 \log_{10}(l_{z_b} \cdot s_{qq_b}/l_{z_r} \cdot s_{qq_r})$ . First, the level of the maxima has increased from 4 dB to 6 dB. Second, a clear trend has been established that the RIBU is the most effective at the lowest  $s'$ , and deteriorates as the  $s'$  increases. Third, the maxima frequency appears to remain unchanged at  $f\delta/U_\infty = 3.5$ . The upper limit of the Amiet noise sources reduction also becomes a function of the logarithmic, instead of behaving linearly, against the frequency, i.e. the spectra now follow the  $14 \log_{10}(f\delta/U_\infty)$  instead of the  $1.5(f\delta/U_\infty)$ .
- (C) The addition of riblets in conjunction with the LEBU<sub>5.0</sub> can revert the upper limit of the Amiet noise sources reduction back to the  $2.5(f\delta/U_\infty)$ , which is an improvement over the LEBU-only case at  $1.5(f\delta/U_\infty)$  as the result of the “counter-balance” effect between the wall pressure fluctuation and lateral coherence length.
- (D) More significantly, the ability to reduce the Amiet noise sources at low frequency by the riblets has been successfully replicated in the RIBU configuration where up to 2 dB reduction can be harnessed when  $s' \geq 2.64$ .
- (E) At  $s' < 2.64$ , however, the addition of riblets seems to be a disadvantage where the otherwise self-similar behaviour is destroyed, and in some cases, a significant enhancement of the Amiet noise sources can be observed.

Generally, the RIBU can improve the self-similar behaviour of the Amiet noise sources spectra, except for the situation in (E) as described above. The RIBU can reduce the Amiet noise source at (A), enhance the maxima of the Amiet noise sources reduction (B), and most importantly, it has a potential to achieve an enhanced noise reduction across a very large range of frequency as demonstrated in (C) and (D).

The performance of the LEBU and RIBU can also be examined in the context of frequency-integrated Amiet noise sources:

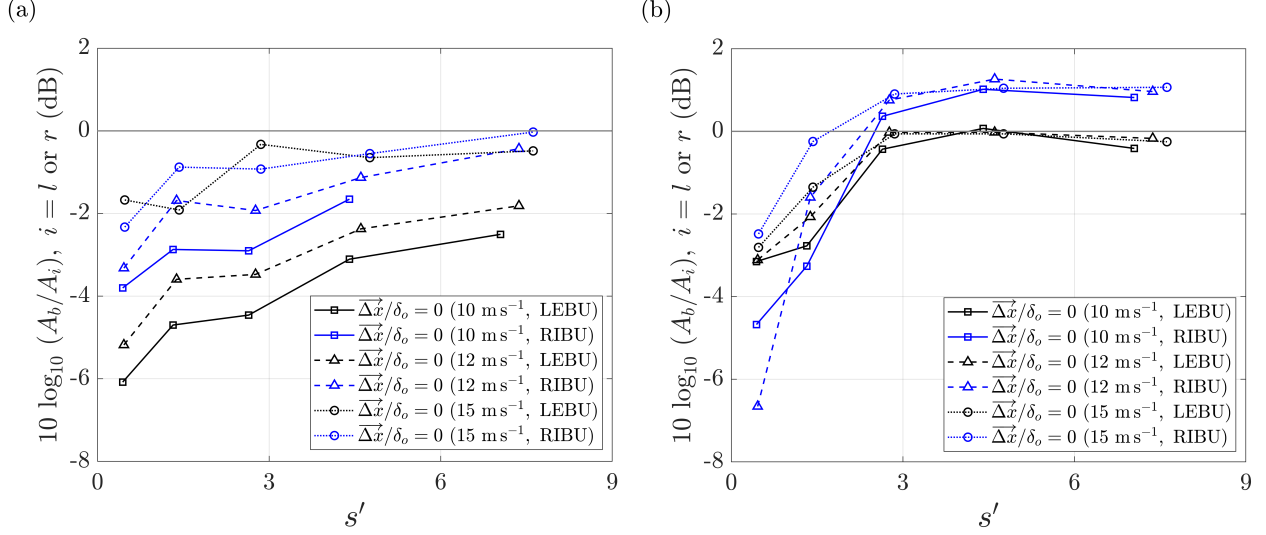


**Fig. 15** Difference in the overall Amiet noise sources,  $10 \log_{10}(A_b/A_i)$ , where  $i = l$  or  $r$ , against  $s'$  for (a) LEBU<sub>2.5</sub> & RIBU<sub>2.5</sub>, and (b) LEBU<sub>5.0</sub> & RIBU<sub>5.0</sub>.

$$A_i = \int_f \left[ l_{zi}(f) \cdot s_{qqi}(f) \right] df, \quad i = b, l \text{ or } r, \quad (4)$$

where  $b$ ,  $l$  and  $r$  refer to the baseline, LEBU and RIBU, respectively. Similarly, the frequency range for the integration is between 0.15 and 6 kHz. Hence, the overall performance of the LEBU and RIBU against  $s'$  can be quantified in the expression of  $10 \log_{10}(A_b/A_l)$  and  $10 \log_{10}(A_b/A_r)$ , as shown in Figure 15.

In Figure 15(a), the trend of a slow recovery towards the baseline level for the overall Amiet noise sources, as  $s'$  increases, is similar to the overall wall pressure fluctuations in Figure 7(a). The RIBU consistently outperforms the LEBU counterparts, except at  $U_\infty = 15 \text{ ms}^{-1}$  where the differences become smaller. In some cases, the LEBU is better than the RIBU. As reported in [6], the capability of the riblets to reduce high frequency Amiet noise sources weakens as the freestream velocity increases. Owing to the thinning of the turbulent boundary layer thickness, the riblets are increasingly behaving as a surface roughness, which is expected to exacerbate the LEBU at  $\tilde{h} = 2.5 \text{ mm}$  whose emanated wake will be close to the wall surface. The combination of these will increase the level of wall pressure fluctuation instead of reducing it. Overall, there is no evidence that the Amiet noise sources can be reduced by either the LEBU or RIBU when the LEBU is placed at  $\tilde{h} = 2.5 \text{ mm}$ .

At  $\tilde{h} = 5.0 \text{ mm}$  for the LEBU, however, the addition of riblets can exert a positive impact to the reduction of overall Amiet noise sources, as shown in Figure 15(b). Both the LEBU and RIBU exhibit good self-similar behaviours. While the LEBU alone can only just manage to maintain  $10 \log_{10}(A_b/A_l) \approx 0$  (due to the counter-balancing of the  $s_{qqi}$  and  $l_{zi}$ ), the RIBU is demonstrated to be capable of achieving an overall reduction of  $10 \log_{10}(A_b/A_r)$  up to 1.5 dB at  $s' > 3$ .

Although the overall reduction appears to be modest at first glance, it is important to state that the current work is a feasibility study, not an optimisation study. There are other influencing parameters that have good potential to further enhance the performance, such as the different riblets designs, different aerofoil shape and size of the LEBU, different trailing edge treatment for the LEBU for the generation of inhomogeneous wake, and different angles of attack of the LEBU relative to the wall surface. The last point is particularly interesting because it can become an active control mechanism to maintain or even enhance the effectiveness of the RIBU in transient flow conditions. Overall, the RIBU has demonstrated good potential as an effective source targeting device to mitigate turbulent noise sources and achieve self-noise reduction. It is hoped that the preliminary results presented here can attract attentions in future research to understand more of the physical mechanisms and exploit further benefits.

## V. Conclusion

A successful mitigation of the Amiet's turbulent noise sources should be underpinned by reductions in both the wall pressure fluctuation and lateral coherence length scale. The Large Eddy BreakUp (LEBU) device, if placed strategically at the outer part of a zero pressure gradient turbulent boundary layer, and  $s' > 3$ , would be able to achieve reductions of the wall pressure fluctuations especially at the mid and high frequency ranges. However, what appears to be the optimal LEBU configuration for the mitigation of wall pressure fluctuation will not be reciprocated fully in the lateral coherence length, where an increase of the length scale across a large range of frequency has been observed when  $s' > 3$ .

While the wall pressure fluctuations is insensitive to the LEBU at low frequency, the lateral coherence length scale at low frequency can even be enhanced if the LEBU is placed at  $s' > 3$ . When the Amiet noise source spectrum is integrated across the frequency to obtain the overall level, contribution from the low frequency component will be the most dominant. Therefore, there might still be a challenge to use the LEBU alone to reduce the overall, frequency-integrated Amiet noise source.

In our previous study, riblets used as a near wall device have been found to reduce both the wall pressure fluctuations and lateral coherence length scales at low frequency. When the riblets and LEBU are used concurrently (RIBU), they can target the turbulent boundary layer independently without much interference against each other. Indeed, the low frequency component of the Amiet turbulent noise sources can be reduced by the RIBU. In addition, reduction of the mid frequency component is further enhanced. Hence, using the RIBU has been shown to reduce the frequency-integrated, overall Amiet noise source, and potentially, the trailing edge noise.

It is well known that LEBU is originally designed to reduce turbulent skin friction. Although a definite proof of net-drag reduction by LEBU remains inconclusive even after more than 40 years of research in the community, LEBU is not expected to increase drag, if any, as significantly as the finlet, serration, and so on. A carefully designed riblets can also yield benefit in the turbulent skin friction reduction. Therefore, the RIBU can be an attractive new concept to wind turbine blades, aircraft engines and so on.

## Acknowledgments

This research was funded, either in whole or in part, by the Engineering and Physical Sciences Research Council in the United Kingdom through research Grant No. EP/N018737/1. The authors would also like to thank the PhD studentship sponsored by the Thomas Gerald Gray Charitable Trust in the United Kingdom.

## References

- [1] Brooks, T. F., Pope, S. D., and Marcolini, M. A., “Airfoil self-noise and prediction,” NASA Reference Publication 1218, Retrieved from: <https://ntrs.nasa.gov/archive/nasa/casi.ntrs.nasa.gov/19890016302.pdf>, NASA Langley Research Center, Hampton (VA), 1989. (Accessed: 2020-04-08).
- [2] Ffowcs Williams, J. E., and Hall, L. H., “Aerodynamic sound generation by turbulent flow in the vicinity of a scattering half plane,” *J. Fluid Mech.*, Vol. 40, No. 4, 1970, pp. 657–670. <https://doi.org/10.1017/S0022112070000368>.
- [3] Amiet, R. K., “Noise due to turbulent flow past a trailing edge,” *J. Sound. Vib.*, Vol. 47, 1976, pp. 387–393. [https://doi.org/10.1016/0022-460X\(76\)90948-2](https://doi.org/10.1016/0022-460X(76)90948-2).
- [4] Howe, M. S., “A review of the theory of trailing edge noise,” *J. Sound. Vib.*, Vol. 61, 1978, pp. 437–465. [https://doi.org/10.1016/0022-460X\(78\)90391-7](https://doi.org/10.1016/0022-460X(78)90391-7).
- [5] Lee, S., Ayton, L., Bertagnolio, F., Moreau, S., Chong, T. P., and Joseph, P., “Turbulent boundary layer trailing-edge noise: Theory, computation, experiment, and application,” *Prog Aerosp Sci*, Vol. 126, 2021, p. 100737. <https://doi.org/10.1016/j.paerosci.2021.100737>.
- [6] Muhammad, C., and Chong, T. P., “Mitigation of turbulent noise sources by riblets,” *Journal of Sound and Vibration*, Vol. 541, 2022, p. 117302. <https://doi.org/https://doi.org/10.1016/j.jsv.2022.117302>.
- [7] Yajnik, K. S., and Acharya, M., “Non-equilibrium effects in a turbulent boundary layer due to the destruction of large eddies,” *Structure and Mechanisms of Turbulence I*, edited by H. Fiedler, Springer Berlin Heidelberg, Berlin, Heidelberg, 1978, pp. 249–260. [https://doi.org/10.1007/3-540-08765-6\\_24](https://doi.org/10.1007/3-540-08765-6_24).
- [8] Hefner, J. N., Weinstein, L. M., and Bushnell, D. M., *Large-Eddy Breakup scheme for turbulent viscous drag reduction*, 1980, pp. 110–127. <https://doi.org/10.2514/5.9781600865466.0110.0127>.
- [9] Savill, A. M., and Mumford, J. C., “Manipulation of turbulent boundary layers by outer-layer devices: skin-friction and flow-visualization results,” *Journal of Fluid Mechanics*, Vol. 191, 1988, p. 389–418. <https://doi.org/10.1017/S0022112088001624>.
- [10] Chin, C., Örlü, R., Monty, J., Hutchins, N., Ooi, A., and Schlatter, P., “Simulation of a Large-Eddy-Break-up Device (LEBU) in a Moderate Reynolds Number Turbulent Boundary Layer,” *Flow, Turbulence and Combustion*, Vol. 98, 2016, pp. 445–460. <https://doi.org/10.1007/s10494-016-9757-y>.

- [11] Chong, T. P. and Muhammad, C., “On the enhancement and suppression of turbulent wall pressure by the Large Eddy BreakUp devices,” *Physics of Fluids*, Vol. 36, No. 4, 2024, p. 045157. <https://doi.org/10.1063/5.0195041>, URL <https://doi.org/10.1063/5.0195041>.
- [12] Walsh, M. J., and Lindemann, A. M., “Optimization and application of riblets for turbulent drag reduction,” *22<sup>nd</sup> Aerospace Sciences Meeting*, 1984. <https://doi.org/10.2514/6.1984-347>.
- [13] Gudilin, I. V., Lashkov, Y. A., and Shumilkin, V. G., “Combined effect of longitudinal riblets and LEBU-devices on turbulent friction on a plate,” *Fluid Dynamics*, Vol. 30, 1995, pp. 366–371. <https://doi.org/10.1007/BF02282448>.
- [14] Gruber, M., “Airfoil noise reduction by edge treatments,” *PhD Thesis, University of Southampton*. , 2012. <https://doi.org/http://eprints.soton.ac.uk/id/eprint/349012>.
- [15] Garcia Sagrado, A. P., “Boundary layer and trailing edge noise sources,” Ph.D. thesis, University of Cambridge, 2008.
- [16] Chong, T. P., and Zhong, S., “On the three-dimensional structure of turbulent spots,” *J Turbomach*, Vol. 127, No. 3, 2005, pp. 545–551. <https://doi.org/10.1115/1.1928286>.
- [17] Schubauer, G. B., and Klebanoff, P. S., “Contributions on the mechanics of boundary-layer transition,” Nasa reference publication 1289, retrieved from: <https://ntrs.nasa.gov/api/citations/19930092285/downloads/19930092285.pdf>, NASA Langley Research Center, Hampton (VA), 1956. (Accessed: 2021-07-05).
- [18] Gostelow, J. P., Melwani, N., and Walker, G. J., “Effects of streamwise pressure gradient on turbulent spot development,” *J Turbomach*, Vol. 118, No. 4, 1996, pp. 737–743. <https://doi.org/10.1115/1.2840929>.